Stable and Reduced-Linewidth Laser Through Active Cancellation of Reflections Without a Magneto-Optic Isolator

Hossam Shoman, Nicolas A. F. Jaeger, Connor Mosquera, Hasitha Jayatilleka, Minglei Ma, Haisheng Rong, *Senior Member, IEEE*, Sudip Shekhar, and Lukas Chrostowski, *Senior Member, IEEE*

***Abstract*—Integrating photonics with CMOS electronics in silicon is essential to enable chip-scale, electronic-photonic systems that will revolutionize classical and quantum communication and computing systems. However, the lack of an on-silicon isolator, capable of blocking unwanted back reflections and ensuring the stable operation of the laser, precluded many previous demonstrations from providing single-chip solutions. For most optical systems employing a laser, magneto-optic isolators have been indispensable, but such isolators are incompatible with silicon. To stabilize on-chip lasers, reflections-cancellation circuits were proposed as a way to reduce the reflections going back to the laser. Yet, a stable laser against time-varying back reflections was never demonstrated. Here we demonstrate a stable quantum well-distributed feedback (QWDFB) laser against slowly time-varying reflections using a reflections-cancellation circuit (RCC) on a foundry-produced, silicon-photonic (SiP) chip. The optical spectrum and the relative intensity noise (RIN) of the laser when the RCC was running is comparable to when an isolator was used. By accurately locking the laser in a stable optical feedback regime, the RCC further enhances the QWDFB laser performance by reducing its linewidth by a factor of 100, down to 3 kHz. Both results are enabled using novel techniques in the design, calibration, tuning, and control of the proposed SiP RCC. The optical insertion loss of the RCC is less than 1.5 dB for reflections smaller than −20 dB and can yield isolation ranges of up to 64 dB. Our device paves the way towards the mass production of fully integrated, low-cost electronic-photonic silicon chips without attaching magneto-optic isolators between the laser and the SiP chip.**

***Index Terms*—Semiconductor lasers, laser stabilization, optical feedback, photonic integrated circuits, narrow-linewidth lasers.**

Manuscript received May 18, 2021; revised July 5, 2021; accepted July 6, 2021. Date of publication July 15, 2021; date of current version October 4, 2021. This work was supported in part by the Natural Sciences and Engineering Research Council of Canada, in part by Intel Corporation, in part by SiEPIC program, and in part by the Faculty of Graduate Studies at the University of British Columbia. *(Corresponding author: Hossam Shoman.)*

Hossam Shoman is with the Department of Electrical and Computer Engineering, University of British Columbia, Vancouver, BC V6T 1Z4, Canada, and with Nokia, New York, NY 10016 USA (e-mail: hoshoman@ece.ubc.ca).

Nicolas A. F. Jaeger and Sudip Shekhar are with the Department of Electrical and Computer Engineering, University of British Columbia, Vancouver, BC V6T 1Z4, Canada (e-mail: nickj@ece.ubc.ca; sudip@ece.ubc.ca).

Connor Mosquera is with the Department of Electrical and Computer Engineering, University of British Columbia, Vancouver, BC V6T 1Z4, Canada, and with Lumentum, Nepean, ON K2J 0P7, Canada (e-mail: connormosquera@ece.ubc.ca).

Hasitha Jayatilleka is with the Department of Electrical and Computer Engineering, University of British Columbia, Vancouver, BC V6T 1Z4, Canada, and with Intel Corporation, Santa Clara, California, CA 95054 USA (e-mail: hasitha.jayatilleka@gmail.com).

Minglei Ma is with the Department of Electrical and Computer Engineering, University of British Columbia, Vancouver, BC V6T 1Z4, Canada, and with Ciena Corporation, Ottawa, ON K2K 0L1, Canada (e-mail: mingleim@ece.ubc.ca).

Haisheng Rong is with Intel Corporation, Santa Clara, California, CA 95054 USA (e-mail: haisheng.rong@intel.com).

Lukas Chrostowski is with the Department of Electrical and Computer Engineering, University of British Columbia, Vancouver, BC V6T 1Z4, Canada, and with Quantum Matter Institute, University of British Columbia, Vancouver, BC V6T 1Z4, Canada (e-mail: lukasc@ece.ubc.ca).

This article has supplementary material provided by the authors and color versions of one or more figures available at https://doi.org/10.1109/JLT.2021.3096460.

Digital Object Identifier 10.1109/JLT.2021.3096460

I. Introduction

INTEGRATING photonics with state-of-the-art nanoelectronics in silicon is key to enabling new revolutionizing computing and communication technologies [1]–[4], as it leverages the well-established CMOS foundries used to manufacture the electronics chips at large-scale with low-cost. Towards this goal, great efforts have been made to integrate all the fundamental photonic building blocks on silicon [2], however, many on-chip solutions have not included the laser on the chip. This is because, for stable laser operation, a non-reciprocal device, optical isolator, attached to the output of the laser is required to break the time-reversal symmetry and allow energy to flow out, but block it from flowing back to the laser. If a tiny fraction of the optical power exiting the laser is reflected back to the laser, depending on the amplitude/phase of the reflections, the laser spectral linewidth can broaden, sidebands can appear in the laser spectrum increasing the laser RIN, and the laser coherency can eventually collapse rendering an unstable laser [5]–[7]. Since silicon has a reciprocal lattice, these isolators are most practically realized using additional materials with asymmetric permittivity tensors, such as magneto-optic materials [8]–[11]. However, besides being bulky, and expensive, integrating magneto-optic materials on silicon requires additional process steps, which increases the overall complexity and cost of fabrication, and has yielded devices with high insertion losses.

Other methods of breaking the reciprocity in silicon include using devices based on non-linear [12]–[19] or spatio-temporal modulation [20]–[24] effects. Devices that use non-linear effects require high optical powers and some of the demonstrated solutions are time-reversal symmetric, i.e., they show reciprocal behaviour when continous wave (CW) light is flowing through

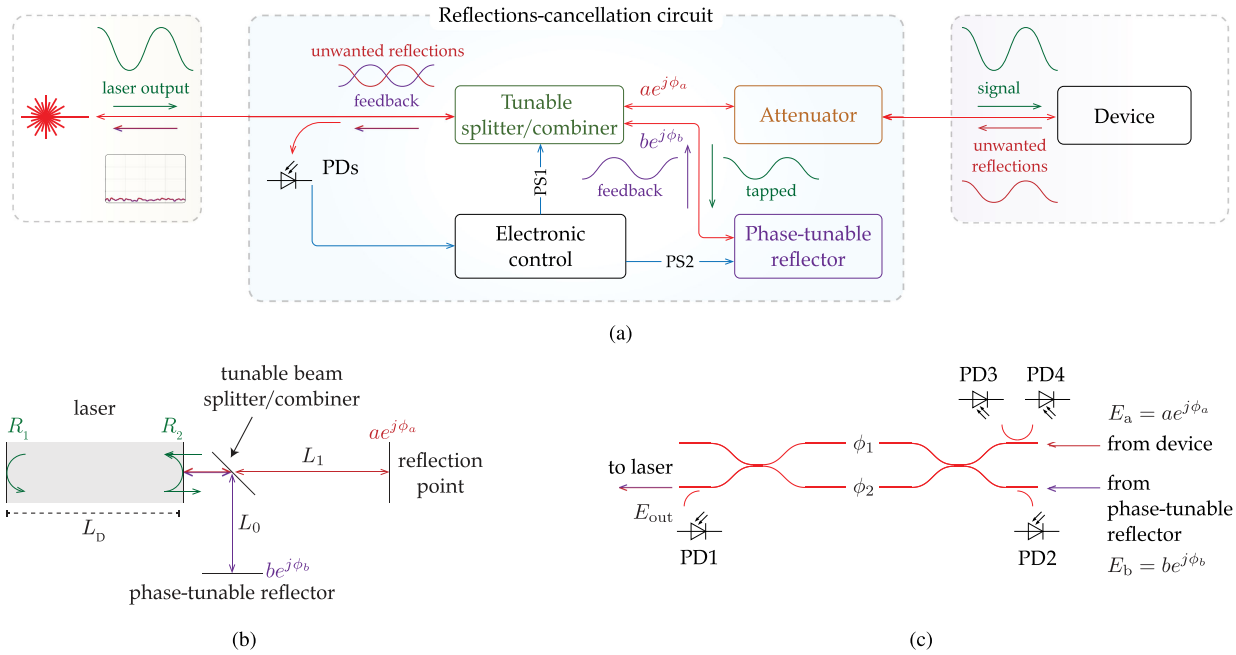

Fig. 1. (a) Conceptual schematic illustrating the RCC. Based on the photocurrents measured by monitoring photodetectors (PDs), a low-speed electronic control actuates the tunable splitter/combiner and the phase-tunable reflector so as to ensure that the feedback to the laser is equal in magnitude to, but in antiphase with, the total unwanted reflections. The attenuator is used to block reflections from the device to the laser, a step which is required in the initial stage of the developed algorithm that simplifies the search for the global minimum from two-dimensions to one-dimension (will be described later in Section IV-C). (b) Free-space illustration of a laser with a reflection point, a tunable beam splitter/combiner, and a phase-tunable reflector. (c) Schematic of the tunable splitter/combiner, which is formed using a 2×2 Mach-Zehnder interferometer (MZI). The power splitting is controlled by changing ϕ_1 using a thermal phase shifter (PS). The location of the PDs shown are selected to ensure accurate amplitude and antiphase matching between the total unwanted reflections and the feedback signal. These PDs are used to monitor: the power flowing to the laser (PD1), the power flowing to the phase-tunable reflector (PD2), fluctuating on-chip reflections (PD3), and the power flowing to the on-chip devices (PD4).

them from both directions simultaneously [13], [19], [25], which limited previous demonstrations to cases in which light was flowing in only one direction at a time. Spatio-temporal modulators require high-speed drive circuits, suffer from high optical losses, and have large footprints, which affect the form factor, power consumption, and overall cost.

In contrast to using isolators, cancelling reflections from going back to the laser can yield a stable laser. A stable laser through reflections cancellation was first proposed and demonstrated using a free-space optical mirror [26]. Recently, integrated circuits were proposed [27]–[31], and a stable laser against moderate parasitic reflections was demonstrated [32] using a tunable reflector in a SiP chip. However, the aforementioned designs precluded the demonstrations from realizing an adequate control loop that would stabilize the laser operation against time-varying reflections with varying levels of amplitudes and phases [32]. Here, through novelties in the design, calibration, tuning, and control of the proposed circuit, we report and demonstrate a new design of an integrated approach toward stabilizing semiconductor lasers in the presence of back reflections. Instead of using an optical isolator, we use a low-speed electronically controlled, SiP RCC to dynamically and actively sense and cancel the light reflected back to the laser [6], [7]. The concept is similar to how active noise-cancelling headphones work, but operates at optical frequencies (∼193 THz) instead of acoustic electrical signals (kHz). Our design enables us to accurately lock the laser in a stable optical feedback regime and deliberately allow a precise finite amount of optical feedback to flow back to the laser, thus resulting in a stable laser and with a reduced spectral linewidth.

The paper is organized as follows, in Section II we describe the principle of operation of the RCC. In Section III, we simulate the laser behaviour with the RCC in the presence of back-reflections. In Section IV, we describe the RCC's integrated design, and discuss the effect of each component in the RCC on the RCC's power cancellation range and loss. We also propose an efficient algorithm that yields a stable laser with time-changing reflections. In Section V, we discuss the chip fabrication and characterization setup. In Section VI, we show the real-time laser stabilization experimental results with the RCC, and conclude by discussing and summarizing our results.

II. The Reflections-Cancellation Circuit

Fig. 1(a) shows the RCC's principle of operation. To block the reflections from going back to the laser, a tunable splitter/combiner and a phase-tunable reflector are used. The tunable splitter taps a portion of the output power leaving the laser and sends it to the phase-tunable reflector. The phase-tunable reflector reflects the tapped power and sets it in antiphase with the total 'unwanted' reflections generated on-chip. The tunable combiner then combines the total unwanted reflections, $ae^{j\phi_a}$, and the feedback reflections, $be^{j\phi_b}$, where a (b) and ϕ_a (ϕ_b) are the magnitude and phase of the field at the tunable combiner top (bottom) input port, respectively. Fig. 1(b) shows a free-space

model of a laser with the equivalent free-space model of the RCC, and Fig. 1(c) illustrates the integrated optic tunable splitter/combiner, which is formed using a tunable 2×2 MZI with 3-dB couplers. Assuming a $50/50$ power coupling ratio for each of the MZI couplers, the optical field going back to the laser (E_{out}) is given by

$$E_{\text{out}} = ae^{j\left(\phi_a + \frac{\phi_1+\phi_2-\pi}{2}\right)} \cos\left(\frac{\Delta\phi}{2}\right) + be^{j\left(\phi_b + \frac{\phi_1+\phi_2-\pi}{2}\right)} \sin\left(\frac{\Delta\phi}{2}\right), \tag{1}$$

where $\Delta\phi = \phi_1 - \phi_2$, and ϕ_1 and ϕ_2 are the phases of the top and bottom arms of the MZI, respectively. To minimize E_{out}, the total unwanted reflections' field going back to the laser should be equal in magnitude to, but in antiphase with, the feedback signal's field going back to the laser, i.e., $a\cos(\frac{\Delta\phi}{2}) = b\sin(\frac{\Delta\phi}{2})$ and $\phi_a = \phi_b + \pi(2m-1), m \in \mathbb{Z}^+$. To achieve these two conditions, a low-speed electronic loop actuates PS1 of the tunable splitter/combiner and PS2 of the phase-tunable reflector based on the photocurrents measured by four PDs.

To precisely monitor the changing reflections' amplitude and phase, four on-chip PDs (PD1-4) were used. PD3 monitors the magnitude of the total unwanted reflections, whereas PD2 monitors the power directed to the phase-tunable reflector. Another photodetector (PD), PD4, is used alongside PD2 to measure the MZI's splitting ratio and ensure the proper scaling of the amplitudes as will be described by the algorithm in Section IV-C. Finally, the antiphase condition is ensured by tracking the power going to the laser using PD1. The attenuator shown in Fig. 1(a) is used only in the initial stage of the algorithm, i.e., the calibration, as will be explained in Section IV-C.

III. Numerical Simulations Using the Lang-Kobayashi Laser Model

To simulate the RCC's effect on the laser temporal response in the presence of back reflections, we refer to Fig. 1(b), which consists of a laser, a reflection point, a beam splitter/combiner, and a reflector. Due to a coherent optical feedback (reflection point), an optical feedback term, $F(t)$, is added to the complex electric field term, $E(t)$, in the standard laser rate equations [7]. Through further simplifications [33], the equations are in a similar form as the Lang-Kobayashi's laser model with optical feedback [7], [34], where

$$\frac{d}{dt}E(t) = \frac{1-i\alpha}{2}\left(g(n(t),|E(t)|^2) - \frac{1}{\tau_{\text{p}}}\right)E(t) + F(t) + E_{\text{sp}}(t), \tag{2a}$$

$$\frac{d}{dt}n(t) = \frac{I}{q} - \frac{n(t)}{\tau_{\text{s}}} - g(n(t),|E(t)|^2)|E(t)|^2 + F_{\text{n}}(t). \tag{2b}$$

In Eq. (2), α is the linewidth enhancement factor, $g(n,|E(t)|^2)$ represents the modal gain which is a function of both the carrier number, $n(t)$, and photon number, $S(t) = |E(t)|^2$ and is expressed in terms of the linear gain, $A_{\text{n}}(n(t) - n_0)$, as [7]

$$g(n(t),|E(t)|^2) = A_{\text{n}}(n(t)-n_0)(1-\kappa_{\text{g}}P(t)), \tag{3}$$

where κ_{g} is the gain saturation coefficient, A_{n} is the modal gain coefficient and can be expressed as $A_{\text{n}} = v_{\text{g}}(\partial g/\partial n)$ where v_{g} is the group velocity of light inside the laser cavity and $\partial g/\partial n$ represent the change in gain with carriers, and n_0 is the carriers number at transparency (when the gain is zero). τ_{p} is the photon lifetime in per unit time, I is the laser bias current, q is the electron charge, and τ_s is the carriers lifetime. $E_{\text{sp}}(t)$ and $F_{\text{n}}(t)$ are the Langevin noise forces, which represent the spontaneous emission and carrier noises, respectively [35], where

$$E_{\text{sp}}(t) = \frac{R}{2E^*(t)} + \frac{E(t)}{|E(t)|}\sqrt{\frac{R}{2\Delta t}}\,(x_e + jx_\phi), \tag{4a}$$

$$F_{\text{n}}(t) = \sqrt{\frac{2|E(t)|^2R}{\Delta t}}x_{\text{e}} + \sqrt{\frac{2n(t)}{\tau_s\Delta t}}x_{\text{n}}, \tag{4b}$$

$$x_{\text{e}} = x_1\cos(\phi(t)) + x_2\sin(\phi(t)), \tag{4c}$$

$$x_\phi = -x_1\sin(\phi(t)) + x_2\cos(\phi(t)), \tag{4d}$$

where R is the the emission rate into the lasing mode, Δt is the time step used in numerically solving Eq. (2), x_1, x_2, and x_{n} are independent Gaussian random variables with zero mean and unity standard deviation, $\langle x_1^2\rangle = \langle x_2^2\rangle = \langle x_{\text{n}}^2\rangle = 1$, and $\phi(t)$ is the light's phase which is given by $\phi(t) = \angle E(t)$. R is expressed as [7]

$$R = \frac{n_{\text{sp}}}{\tau_{\text{p}}}\left[\frac{(\sqrt{R_1}+\sqrt{R_2})(1-\sqrt{R_1R_2})}{\sqrt{R_1R_2}\ln(1/R_1R_2)}\right]^2, \tag{5}$$

where R_1 and R_2 represent the power reflection coefficient at each of the laser facets, and n_{sp} represents the inversion factor. The optical feedback term in Eq. (2), $F(t)$, is expressed as,

$$F(t) = \frac{1}{\tau_{\text{D}}}\frac{1-R_2}{\sqrt{R_2}}\left(-F_0(t) + F_1(t)\right), \tag{6a}$$

$$F_0(t) = E(t-\tau_0)\kappa^2be^{j\omega_0\tau_0}e^{j\phi_b}, \tag{6b}$$

$$F_1(t) = E(t-\tau_1)(1-\kappa^2)ae^{j\omega_0\tau_1}e^{j\phi_a}, \tag{6c}$$

where τ_{D} is the light's round-trip time to travel between the laser facets, which is expressed as $\tau_{\text{D}} = 2n_{\text{g}}L_{\text{D}}/c$, where n_{g} is the laser cavity's group index, L_{D} is the laser cavity length, and c is the speed of light in free-space. τ_1 is light's round-trip time to travel between the laser right facet and reflection point, which is given by $\tau_1 = 2n_{\text{g},1}L_1/c$, where $n_{\text{g},1}$ is the group index of the medium between the laser and the 'unwanted' reflection point, L_1 is the distance between the laser and the 'unwanted' reflection-point. ω_0 is the laser angular optical frequency which is expressed as $\omega_0 = 2\pi f_0 = 2\pi c/\lambda_0$, f_0 is the laser temporal frequency, and λ_0 is the free-space wavelength. $\tau_0 = 2n_{\text{g},1}L_0/c$ is the roundtrip-time between the laser and the phase-tunable reflector, where L_0 is the distance between the laser and the phase-tunable reflector. The negative sign added before $F_0(t)$ in Eq. (6a) accounts for the $\pi/2$ phase shift due to the beam splitter/combiner as light passes through it twice thus undergoing

TABLE I
LASER PARAMETERS USED IN SOLVING EQ. (2) IN ACCORDANCE WITH REF. [7]

Param.	Description	Value
λ_0	laser emission wavelength	1.55 µm
n_g	medium group index of laser cavity	4.5
$n_{g,1}$	medium group index of laser to reflection	1
L_D	length of laser cavity	300 µm
R_1	laser left facet power reflectivity	0.32
R_2	laser right facet power reflectivity	0.32
A_n	modal gain coefficient	2.2×10^3 s^{-1}
n_0	carrier number at transparency	2×10^8
κ_g	gain saturation coefficient	3.5 W^{-1}
n_{sp}	semiconductor incomplete inversion factor	2
τ_s	carrier lifetime	2 ns
α	linewidth enhancement factor	6
α_s	scattering loss in the active volume	3.6×10^3 m^{-1}
L_0	laser to phase-tunable reflector distance	1 mm
L_1	laser to reflection point distance	21 mm
P_{ss}	steady-state output power per facet	5×10^{-3} W

a π-phase shift. κ^2 is the power splitting/combining coupling coefficient of the beam splitter/combiner.

Eq. (2) is a delay-differential equation which can be solved numerically using the Runge-Kutta method of the fifth order (RK5) [33], [36]. We use a fixed step-size of 10 ps in our calculations, which ensures a white spectrum of the noise forces in Eq. (4) up to 44 GHz, which is above the laser relaxation frequency (∼3 GHz) [35], [37]. The calculations were carried out using the parameters in Table I which are in accordance with ref. [7].

In Table I, P_{ss} refers to the desired output power exiting each of the laser facets at steady-state, which is written in terms of E_{ss} as

$$|E_{ss}|^2 = \frac{2P_{ss}\tau_p}{hf_0}, \tag{7}$$

where h is Planck's constant. Eq. (7) is valid for the case in which $R_1 = R_2$. We use the desired output power, P_{ss} value to calculate the bias current, I, which can be found by solving Eq. (2) for n_{ss} (the carrier number) and I at steady-state without the feedback or noise terms, which yields $I = 46.7$ mA and $n_{ss} = 4.28 \times 10^8$. Before simulating the optical feedback effect on the laser, we first solve Eq. (2) (without optical feedback or noise) using an initial value of 1 and 0 for the number of photons and carriers, respectively, and then run the simulation using a fixed step size of 1 ps for 50 ns in response to a current step-function. We then save the last value of the field and the carrier number and use it as the new initial value to Eq. (2) when we add the optical feedback term. We set $L_0 = 1$ mm (typical distance of the circuit from a laser integrated on-chip), and $L_1 = 21$ mm (arbitrary distance of an on-chip reflection point). We also set the power reflection coefficients to -30 dB ($a^2 = b^2 = 10^{-3}$, where a and b are the fields reflection coefficients due to the 'unwanted' reflection point and the phase-tunable reflector, respectively), and accordingly $\kappa^2 = 0.5$, corresponding to a 50/50 splitter/combiner (although in reality a should be set to 1 and κ^2 should be varied, however, here, we match the reflection amplitudes by setting both reflections to the same value), and sweep ϕ_b from 0 to 2π. Fig. 2(a) shows the change in the average

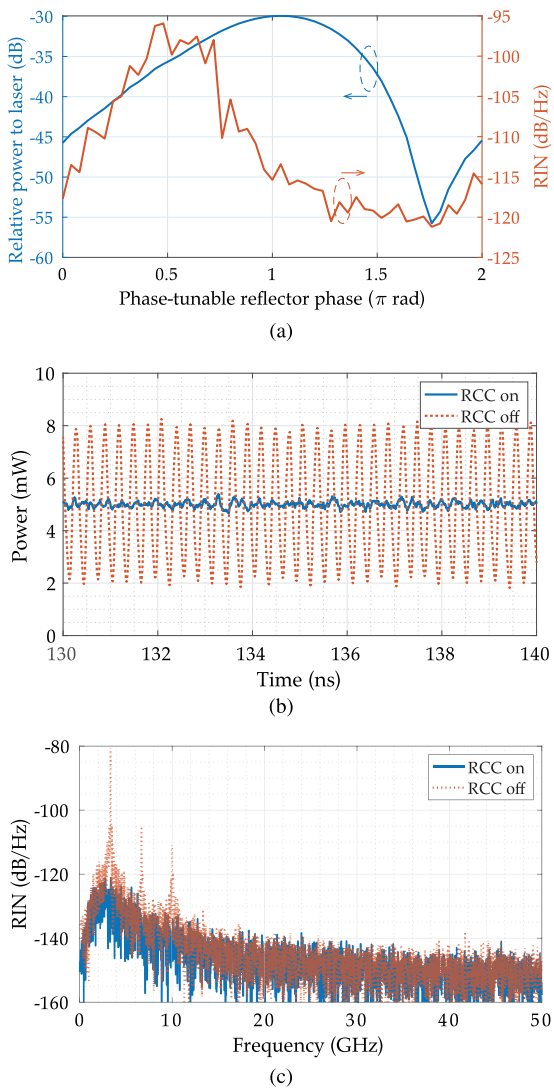

Fig. 2. Numerical simulation results. (a) Change in the relative power going back to the laser and the maximum RIN (maximum in the spectrum from 0–50 GHz) as a function of the phase-tunable reflector's phase, ϕ_b. (b) The simulated laser temporal response, and (c) the RIN spectrum when the RCC is turned off (-30 dB reflections going back to laser) and when the RCC is on (reflections are minimized to -55 dB).

relative power going back to the laser as a function of ϕ_b, which can be written as $\langle P(t)_{\text{to laser, relative}}\rangle / P_{ss}$, where

$$\langle P(t)_{\text{to laser, relative}}\rangle = \left\langle \frac{hf_0| - F_0(t) + F_1(t)|^2}{2\tau_p} \right\rangle. \tag{8}$$

To capture the power going back to the laser, we save $F_0(t)$ and $F_1(t)$ at every time step Eq. (2) is solved. When $F_0(t)$ and $F_1(t)$ are in antiphase with each other, the power going back to the laser is minimal (-55 dB). This happens at $\phi_b = 1.76\pi$ rad. In such a case, the maximum RIN (maximum over the frequency range of 0–50 GHz which is at the laser relaxation frequency) is minimal, at -120 dB/Hz as shown in Fig. 2(a). The RIN is expressed as [38]

$$\text{RIN} = \frac{\langle \delta P^2(t)\rangle}{\langle P(t)\rangle^2}, \tag{9}$$

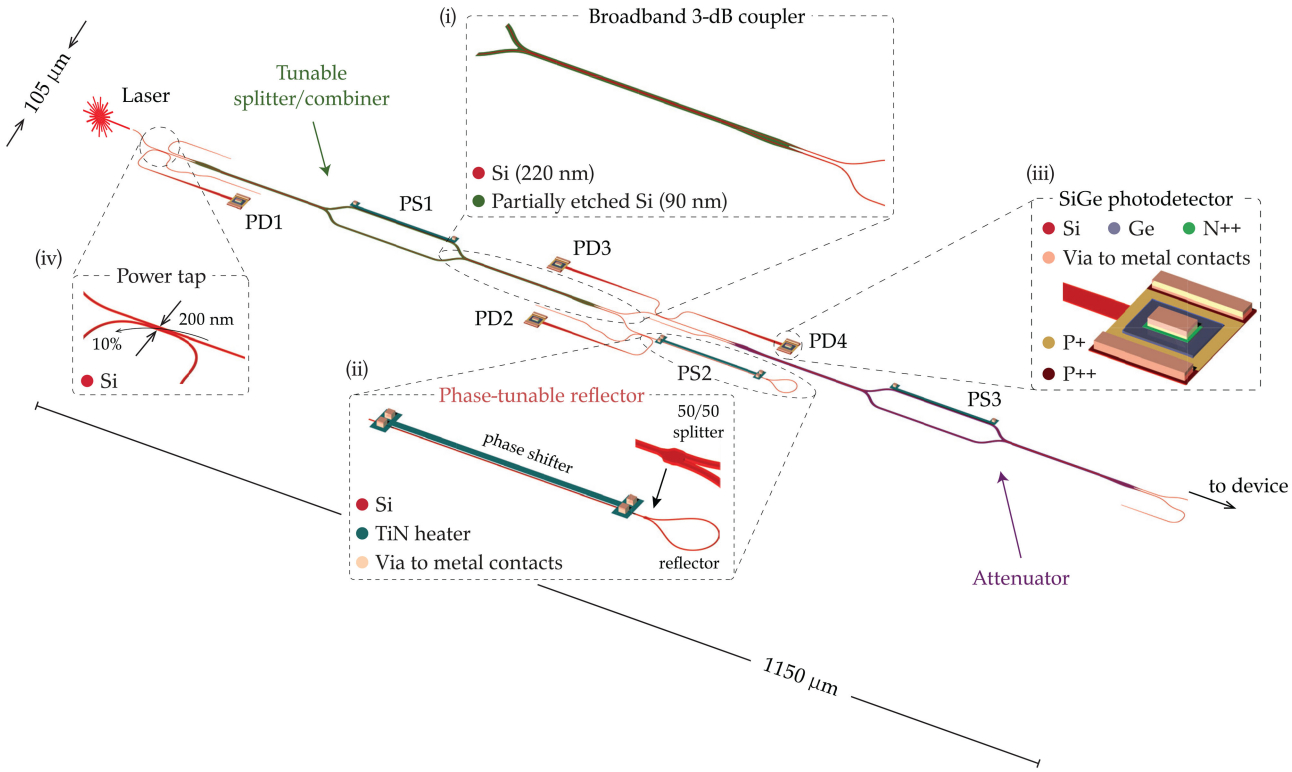

Fig. 3. Layout of the RCC illustrating its components. The tunable splitter/combiner is formed using an MZI with (i) broadband 3-dB couplers and a TiN heater on top of one of the MZI arms. The (ii) phase-tunable reflector is formed using a PS, a Y-junction to split and combine light, and a bent waveguide loop. The attenuator is formed using an MZI similar to the one used in the tunable splitter/combiner which results in 42 dB of attenuation when turned on. (iii) The four SiGe PDs (PD1-PD4) were connected to (iv) 10% power taps.

where $\langle \delta P^2(t) \rangle$ is the laser mean-square optical intensity fluctuation in a 1-Hz bandwidth and $\langle P(t) \rangle^2$ is the laser average optical power [38]. Fig. 2(b) and Fig. 2(c) shows the simulated temporal response and the RIN of the laser, respectively, when the RCC is off (-30 dB of reflections going back to the laser) and when the RCC is on ($F_0(t)$ and $F_1(t)$ are going back to the laser and $\phi_b = 1.76\pi$ rad). When the RCC is off, the laser self-pulsates and the maximum RIN increases to -80 dB/Hz. However, when the RCC is on, the laser temporal response is stable with time ($\sim$5 mW) and the maximum RIN is reduced to -120 dB/Hz. This indicates that through matching the amplitude of the feedback signal to that of the reflections' and by setting them in anti-phase with each other, a stable laser can be obtained.

IV. Integrated Reflections-Cancellation Circuit Design

Fig. 3 shows the layout of the RCC. The tunable splitter/combiner is formed using an MZI with a PS (PS1) above one of the MZI arms. The MZI couplers are broadband adiabatic 3-dB couplers [39]. The phase-tunable reflector is formed using a PS (PS2) and a reflector consisting of a compact Y-junction [40] and a waveguide-loop connecting the Y-junction's splitting/combining ports. The PDs are SiGe-based [41] with a measured responsivity of 0.8 A/W and a noise-equivalent power (NEP) of 42.6 pW/$\sqrt{\text{Hz}}$, indicating that optical powers above -73.7 dBm can be detected (using our source-measure unit (SMU)) when the photocurrent is integrated over 0.5 seconds [42] (see Section IV-A for details). The optical attenuator is formed using an MZI, similar to the tunable splitter/combiner. The fixed power taps for the PDs are designed using a directional coupler with 10 μm radius Bezier bends, optimized for low loss [43]. The directional coupler is formed using two 500 $\times$ 220 nm strip silicon waveguides buried in SiO_2 and has a coupling length and gap of 4.394 μm and 200 nm, respectively, to obtain 10% power coupling. The estimated loss per power tap in such a case is 0.46 dB.

A. Power Tap Design and Maximum Power Cancellation by the RCC

In this subsection, we explain the rationale behind the choice of the power taps' power coupling coefficient and its effect on the maximum power cancellation of the RCC. Power taps with fixed power coupling coefficients (κ^2) guide a small portion of the transmitted light to the PD. Note that κ^2 defined in this section is different than κ defined in Section III. A larger κ^2 results in a larger photocurrent readout from the PDs and, thus, increases the reflected power cancellation range, yet decreases the total power going to the subsequent on-chip devices. Therefore, to decide on κ^2, we calculate the minimum reflected power cancelled as a function of κ^2. The maximum power cancelled by the RCC is a function of the PD NEP (minimum optical power that can be detected) and κ^2. The minimum optical power that can detected

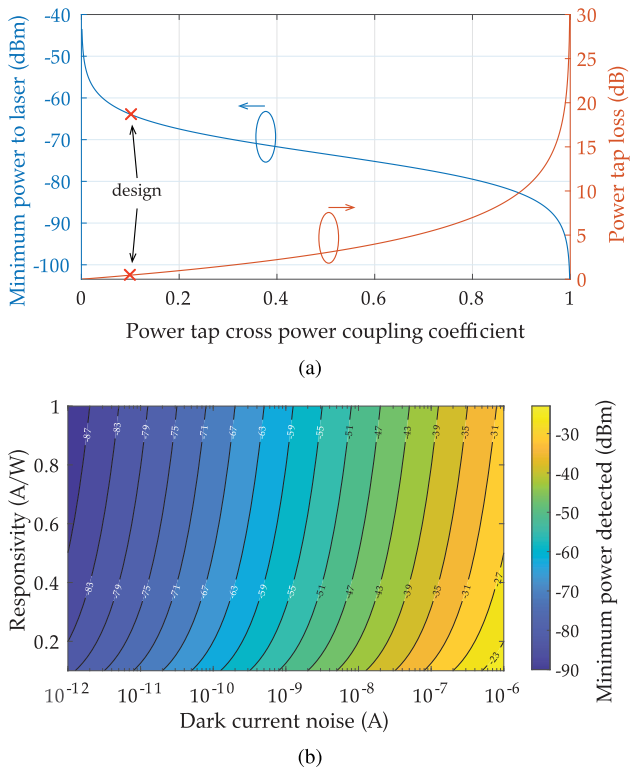

Fig. 4. Maximum power cancelled by the RCC. (a) The simulated minimum power going back to the laser (using Eq. (11)) and the corresponding power tap optical loss as a function of κ^2. (b) The calculated minimum power detected by PD1 as a function of the dark current noises and the responsivities. The power taps can be designed for a specific κ^2, using Eq. (11), for a desired minimum power going back to the laser and an acceptable power tap loss.

by PD1, $\min\{\text{PD1}\}$, is given by the NEP [42], [44],

$$\text{NEP} = \frac{I_{\text{noise}}/\sqrt{\text{Hz}}}{\mathcal{R}} \tag{10}$$

where I_{noise} is the PD's dark current noise measured over a 1 Hz bandwidth (0.5 seconds of integration time) and $\mathcal{R}$ is the PD's responsivity. The minimum optical power going back to the laser, $\min\{P_{\text{out}}\}$, assuming a lossless power tap coupler can then be expressed as

$$\min\{P_{\text{out}}\} = \text{NEP} \cdot \frac{1-\kappa^2}{\kappa^2}. \tag{11}$$

For the PDs used here, we measured the dark current noise and the responsivity. At a bias of -1 V, $I_{\text{noise}} = 34.1$ pA (the root-mean-square deviation of the measured dark current noise from the root-mean-square dark current) and $\mathcal{R} = 0.8$ A/W (see Appendix B). Accordingly, from Eq. (10), the NEP of the PD is 42.6 pW$/\sqrt{\text{Hz}}$. The integration time set on the SMU was 0.5 seconds (1 Hz). The minimum power that can be detected by PD1 is thus $\min\{\text{PD1}\} = -73.7$ dBm when the photocurrent is integrated over 0.5 seconds using our SMU. Using these values, a plot of Eq. (11) is shown in Fig. 4(a). Setting κ^2 to 0.1, $\min\{P_{\text{out}}\}$ at the best cancellation is -64 dBm. This means minimizing the photocurrent measured by PD1 when the laser outputs 0 dBm will result in 64 dB cancellation. For typical laser parameters, cancellation of a feedback ratio exceeding 40 dB can place the laser in the stable 'third' optical feedback regime [7], where the laser remains stable and its linewidth will be narrower than the QWDFB laser free-running linewidth [45]. The resulting loss per power-tap coupler will be 0.46 dB. However, since the feedback required to destabilize the laser can depend on several laser parameters (as explained in ref. [7]), in Fig. 4(b) we show the minimum power detected by PD1 for various PD dark current noises and responsivities. The power taps can be designed for a specific κ^2 (using Eq. (11)), for a desired minimum power going back to the laser and an acceptable power tap loss.

B. RCC Losses and Isolation Ratio

Two sources contribute to the total optical loss of the RCC: 1) a static loss which is fixed by design, and 2) a dynamic loss that changes with the unwanted reflections amplitude. The static loss is dominated by the two power taps that tap a portion of the optical power going to the devices to the PDs. Other sources include the directional couplers and the bends forming the tunable splitter/combiner. If the static loss due to the latter is assumed to be negligible, the static loss (in decibels) is given by

$$\text{static loss} = -20\log_{10}\left(1-\kappa^2\right). \tag{12}$$

Since the power tapped by the RCC should be equal in magnitude to the amount of unwanted reflected optical power ($R_{\text{dB}} = 10\log_{10}|a|^2$), the optical power loss by the RCC will vary as R_{dB} changes, which we define as the dynamic loss, and is expressed as,

$$\text{dynamic loss} = 10\log_{10}\left(\frac{10^{R_{\text{dB}}/10}-1}{10^{R_{\text{dB}}/20}-1}\right). \tag{13}$$

Accordingly, the total optical loss is the sum of the static and dynamic losses.

A plot of the optical losses is shown in Fig. 5. In Fig. 5(a), we show the dynamic loss, the total loss when a 1% power tap is used, and the total loss when a 10% power tap is used (what we used in our design). If 1% power taps were used in our design, the minimum power going back to the laser would be -53 dBm (see Fig. 4(a)), which is sufficient for stabilizing the laser, and the total optical loss in such a case will be $\sim$0.5 dB for cancelling reflections of less than -20 dB. Fig. 5(b) shows the dynamic loss only (due to the RCC tunable splitter/combiner) versus isolation for various output laser powers. Here, the isolation is calculated as the difference between the reflections amplitude and $\min\{P_{\text{out}}\}$ of -64 dBm.

C. One-Dimensional Dynamic Cancellation Algorithm

The algorithm shown in Fig. 6 was used to ensure that the power going back to the laser is minimized by maintaining an equal magnitude and antiphase relationship between the unwanted reflections and the feedback signal. The algorithm is divided into two parts. The first part is a calibration stage which requires running only once, whereas, the second part runs indefinitely to ensure the power going back to the laser is always minimized.

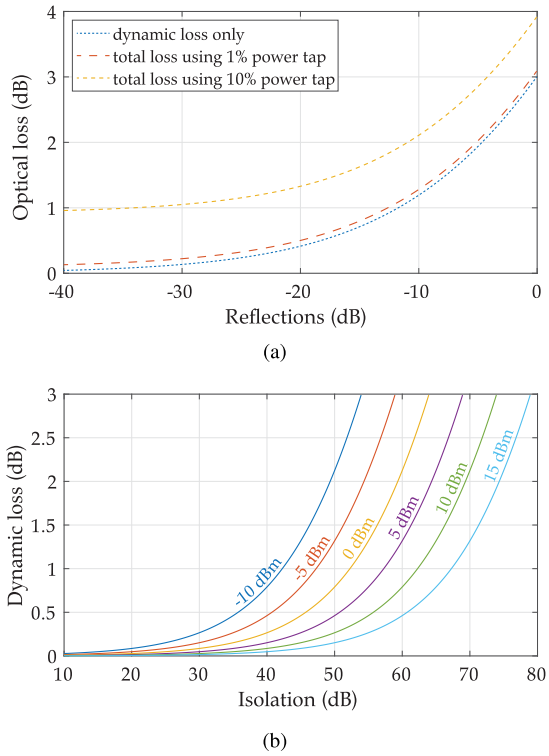

Fig. 5. RCC loss. (a) The optical loss due to the RCC versus reflections to the laser. Shown in the subfigure are the dynamic loss, the total loss when a 1% power tap is used, and the total loss when a 10% power tap is used (what we used in our design). (b) The dynamic loss only (due to the RCC power tapping) versus the isolated/cancelled reflections when the minimum power going to the laser is set to -64 dBm (based on the designed power tap and the PD specifications), for various laser output powers. The laser output power is indicated by the corresponding label on each plot.

First, the magnitude of the unwanted reflections is measured by tuning PS1 to direct the laser light to the device. When I_{PD2} is minimized, I_{PD1} and I_{PD4} values are saved as a_1 and a_4, respectively. The attenuator is then set to maximum attenuation and the tunable splitter/combiner is tuned until the tapped power going to the phase-tunable reflector and back to the laser is equal in magnitude to the unwanted reflections going into the laser (in step 1). This condition is achieved when

$$I_{\mathrm{PD}_1} = \frac{a_1}{a_4} \frac{(I_{\mathrm{PD}_4})^2}{I_{\mathrm{PD}_2} + I_{\mathrm{PD}_4}}. \tag{14}$$

Upon restoring the attenuator (turning it off), the unwanted reflections can then flow to the laser, and PS2 is tuned until I_{PD1} is minimized. The currents measured by PDs PD1, PD2, PD3, and PD4 are then saved as b_1, b_2, b_3, and b_4, respectively. This completes the initial calibration of the RCC. Once calibrated, both PSs, PS1 and PS2, can then be locked to ensure a minimum photocurrent measured by PD1. If the unwanted reflections' magnitude, phase, or both change, I_{PD1} will exceed b_1. To ensure that the power going back to the laser is minimized, the magnitude of the unwanted reflections and feedback signal going into the laser are made equal by tuning PS1 until the following condition is satisfied,

$$I_{\mathrm{PD}_2} = b_2 \sqrt{\frac{I_{\mathrm{PD}_3} I_{\mathrm{PD}_4}}{b_3 b_4}}. \tag{15}$$

PS2 is then locked when I_{PD1} is minimized. The algorithm was tested in Lumerical INTERCONNECT by simulating the RCC (shown in Fig. 3) for the case of -10 dB reflected power with an arbitrary phase shift of 90-degrees. The device generating the unwanted reflections was formed using an MZI (as shown in Fig. 7). The sweep results of the algorithm steps are shown in Fig. 6 beside each corresponding step in the algorithm.

V. Chip Fabrication and Characterization

The chip was fabricated on a 220-nm silicon-on-insulator (SOI) platform using 193 nm-deep ultraviolet lithography at the AMF foundry in Singapore [46], accessed via CMC Microsystems. All the devices used in this work comply with the fabrication rules without any change to the process. Fig. 7 shows an optical microscope image of the fabricated SiP chip containing the RCC. The on-chip device generating 'unwanted' reflections consists of a VOA and a reflector similar to that used in the RCC, which control the magnitude and the phase of the unwanted reflections, respectively. The RCC measures $1150\ \mu\mathrm{m}$ by $105\ \mu\mathrm{m}$, however, this footprint can be minimized with more compact 3-dB couplers [47].

The fabricated chip was assembled in a custom designed FR-4 printed circuit board (PCB) and the on-chip pads were connected to the PCB pads via aluminum wirebonds. The PCB was placed on a 6-axis controlled stage and connected to two 2-channel SMUs (Keithley 2602) and 6 channels of a multi-voltage source (MVS) unit (NI PXIe-6738). Python software, installed on a personal computer, was used to implement the algorithm described in Section IV-C for controlling the RCC PSs (PS1 and PS2) by controlling the MVS unit based on the photocurrents measured by the 4 PDs using the 4 SMU channels. A polarization-maintaining (PM) lensed fiber with an AR coating (that had a return loss of less than 50 dB) was placed on a 6-axis controlled stage and used to couple light into the transverse-electric (TE) mode of the on-chip inverse-taper edge coupler. To test the RCC a commercial QWDFB laser, modified by removing its isolator, was used. The laser was biased at twice the threshold in accordance with ref. [6] to demonstrate the lowest feedback levels for which the RCC was able to stabilize the laser (since the feedback required to destabilize the laser increases with an increased laser output power [7]).

Fig. 8 shows the experimental setup that was used to measure and compare a QWDFB laser optical spectrum, RIN, linewidth, and bit errors with a magneto-optic isolator and without a magneto-optic isolator but with the RCC either disabled (RCC off) or enabled (RCC on). To align the lensed fiber to the RCC input, a 4-channel fiber array was aligned to on-chip calibration grating couplers using a tunable laser (Agilent 81682 A) and a power sensor (Agilent 81635 A). The grating coupler loss was $\sim$5 dB. Then, the fiber array was aligned to the grating coupler placed after the device (see Fig. 7). This was achieved

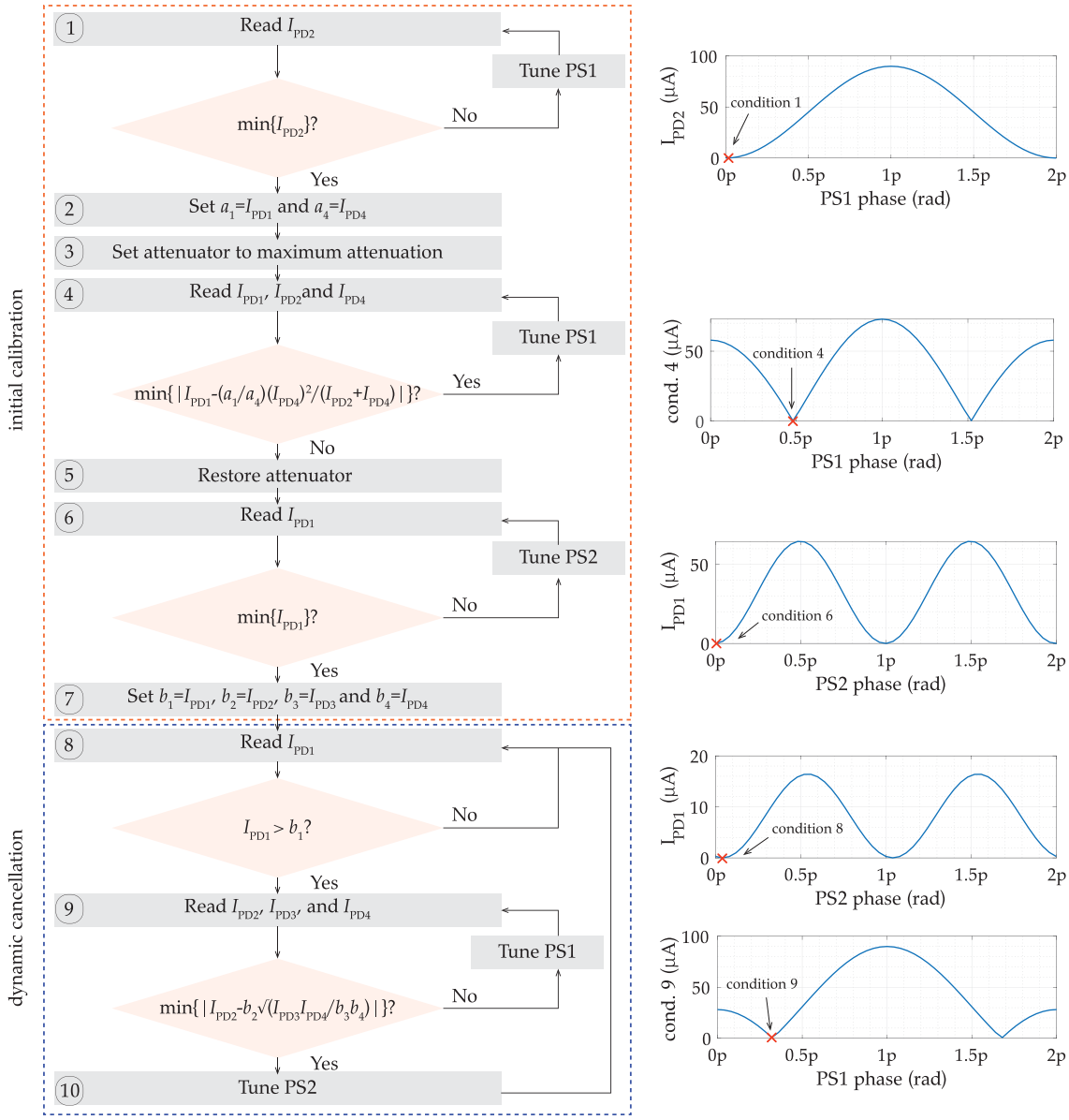

Fig. 6. Dynamic cancellation algorithm. Flow diagram of the control algorithm for the cancellation of unwanted reflections. The steps enclosed in the dashed orange box (top) are used for calibrating the RCC, whereas the steps enclosed in the dashed blue box (bottom) are for real-time (dynamic) reflections cancellation. The plots on the right are the Lumerical INTERCONNECT simulation results. The laser output power was set to 1 mW and the responsivity of the PDs were set to 1 A/W.

by setting the routing MZI (MZI1) to route light from an input grating coupler through the RCC to the output grating coupler. After the fiber array was aligned, the routing MZI was then set to route light from the lensed fiber through the RCC to the output grating coupler. The lensed fiber's position was optimized so that the reflection due to the fiber/chip interface was below −45 dB. The fiber-to-chip coupling loss was ∼11 dB. When conducting the high-speed tests, the high-speed signal was limited to psuedo-random binary sequence (PRBS)-7 because of the bandwidth-limited RF splitter (0.5 GHz - 26.5 GHz) which was used to split the electrical signal to the error detector (ED) and the oscilloscope.

VI. Experimental Results

A. Real-Time Laser Stabilization

Before conducting the experiments, each of the MZIs shown in Fig. 7 were tuned and their cross-transmissions were mapped by monitoring the optical power exiting the output grating coupler. MZI1 (routing MZI) was then biased at 25 mW to route light from the edge coupler to the RCC. MZI2 is the RCC's tunable splitter/combiner and was varied between 25–55 mW. MZI3 acts as the attenuator (42 dB of attenuation), and its phase shifter (PS3) was set to 30 mW when it was turned off, and 0 mW when the attenuator was turned on (only in the

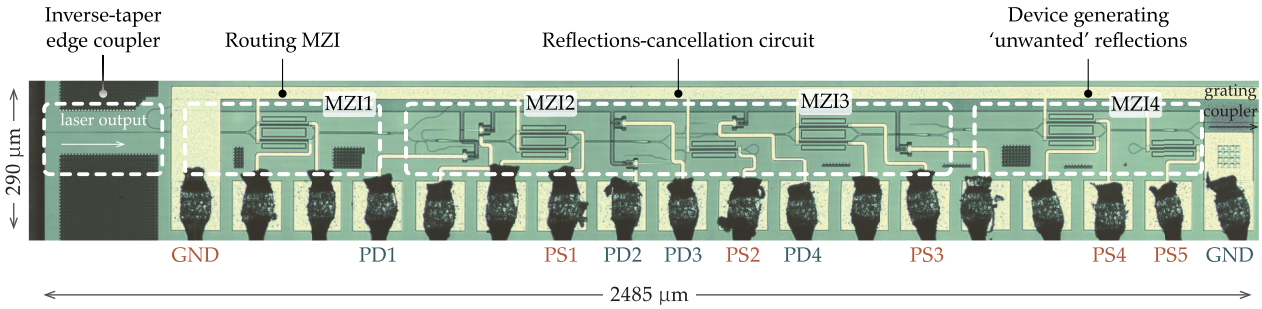

Fig. 7. Microscope image of the fabricated SiP chip which contains the RCC. Additional components include an inverse-taper edge coupler for coupling light from an anti-reflection (AR) coated lensed fiber to the SiP chip and vice-versa, a routing MZI (MZI1), and a device for generating 'unwanted' reflections to the laser, which can generate any magnitude (using PS4 in MZI2) and phase (using PS5) of the reflections. GND, ground.

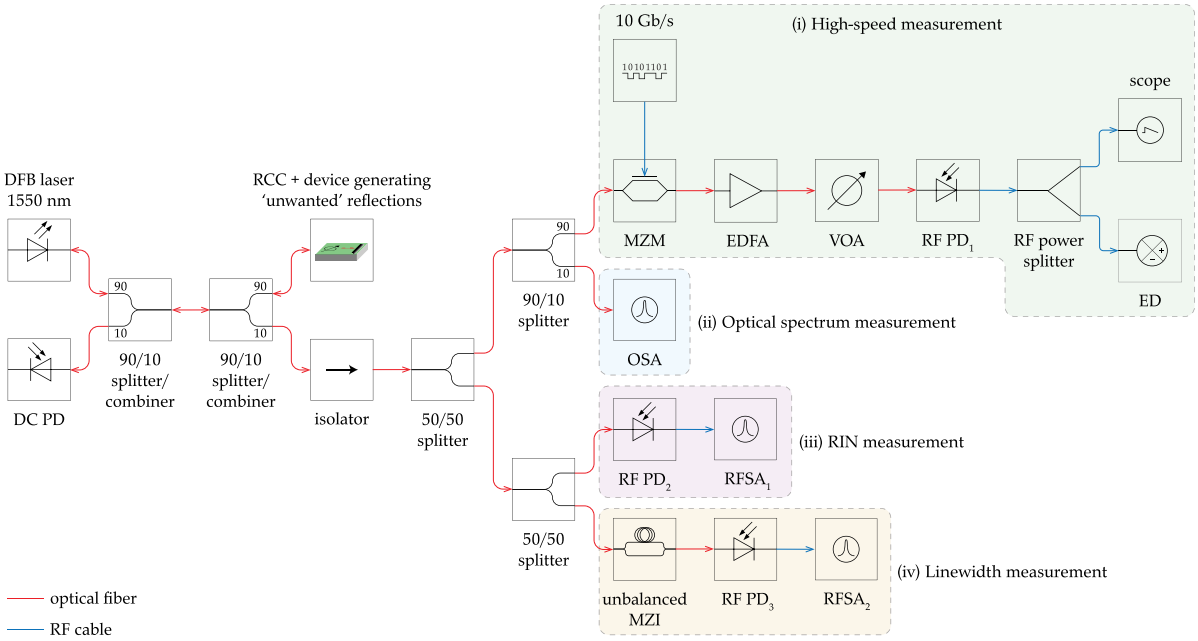

Fig. 8. Experimental setup used for measuring the laser performance. Four experiments were conducted to measure the QWDFB laser performance. (i) A high-speed test, where the on-chip reflections were deliberately changed over time and ~ -14 dB of the laser output was externally modulated using an Mach-Zehnder modulator (MZM) at 10 Gb/s. The optical signal was then amplified using an erbium-doped fibre amplifier (EDFA) and passed through a variable optical attenuator (VOA) into a high-speed PD. An radio-frequency (RF) power splitter was then used to split the electrical signal to an oscilloscope and an error detector (ED) to capture the eye diagrams and count the bit errors, respectively. This test was conducted twice, once with the RCC off and once with the RCC on. (ii) ~ -24 dB of the laser output was coupled to an optical spectrum analyzer (OSA) to measure the optical spectrum of the laser output. (iii) The RIN was measured using a lightwave signal analyzer, where ~ -17 dB of the laser output was incident on a high-speed PD, followed by a calibrated RF spectrum analyzer (RFSA). (iv) The laser linewidth was measured by coupling ~ -17 dB of the laser output into an imbalanced MZI interferometer with a 25 μs delay between the MZI's arms, and the output was then passed on to a high-speed PD and then into an RFSA. The red lines indicate optical fibers and the blue lines indicate electrical RF coaxial cables. The DC PD shown in the left was used to monitor the reflections going back to the laser. The coupling losses between the laser and the SiP chip was $\sim$12 dB. The optical fibers between the laser and the SiP chip were polarization-maintaining fibers (including the lensed fiber). All of the couplers used in the setup were fiber-optic couplers. DC, direct-current.

calibration section of the algorithm shown in Fig. 6). MZI4 acts as a VOA and controls the unwanted reflections magnitude similarly to MZI1 in Fig. 3. For large reflections, MZI4 is set to the 'through' state where all of the power is routed to an on-chip mirror providing the maximum possible reflection to the input port. Whereas for small reflections, MZI4 is set to the 'cross-state' where the optical power is routed to an on-chip grating coupler with minimal reflection providing the minimum possible reflection to the input port. By controlling the amount of light directed to each of its output ports, MZI4 can be used to achieve any amount of reflection between the maximum and minimum possible reflections. MZI4 was swept between 30 mW and 50 mW to reflect -9 to -2 dB of the power going to the on-chip devices.

Fig. 9 illustrates a simplified illustration of the measurement setup showing the optical power at various points in the setup and in the chip. Before turning the RCC on, the reflections on-chip were set to -9 dB and the RCC was calibrated using the algorithm shown in Fig. 6. The calibration results of the algorithm are shown in Fig. 10. After calibration, PS2 was set

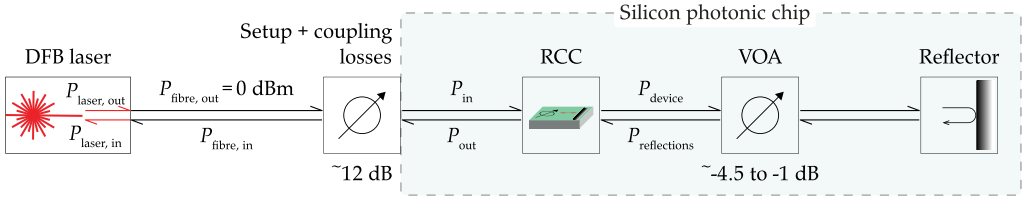

Fig. 9. A simplified illustration of the measurement setup showing the optical power at different points in the link. The laser was biased at 12 mA (twice the threshold) producing an optical power of 1 mW, $P_{\text{fiber, out}} = 0$ dBm. Accounting for the setup and lensed-fiber-to-chip coupling losses, the optical power on the chip going to the RCC (P_{in}) was ~ -12 dBm. The on-chip reflections were varied between -9 and -2 dB using an on-chip VOA and a reflector. The VOA is formed using an MZI, similar to either of the MZIs in Fig. 3.

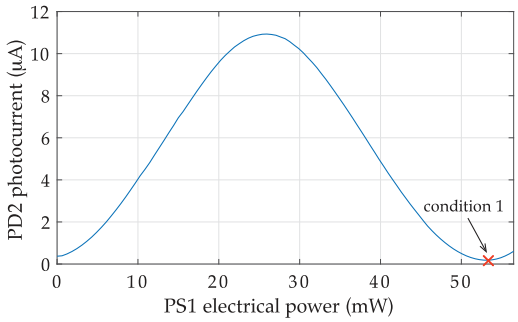

(a)

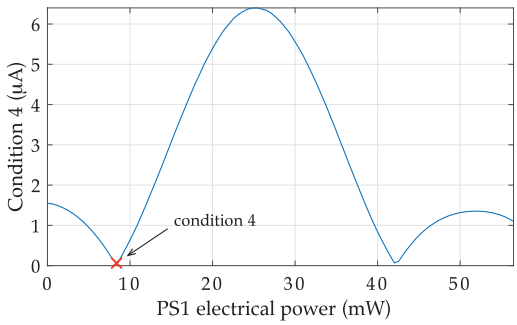

(b)

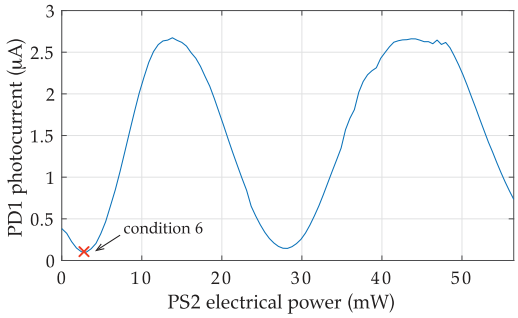

(c)

Fig. 10. Experimental results of the initial calibration part of the dynamic cancellation algorithm. (a) step 1, (b) step 4, and (c) step 6 of the algorithm shown in Fig. 6.

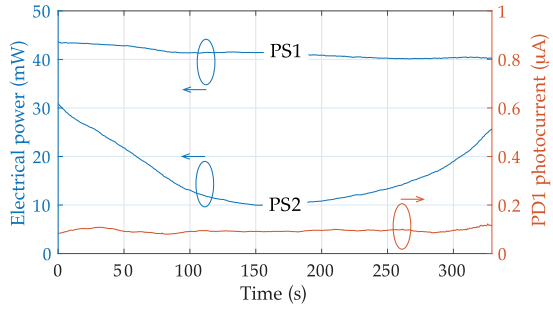

(a)

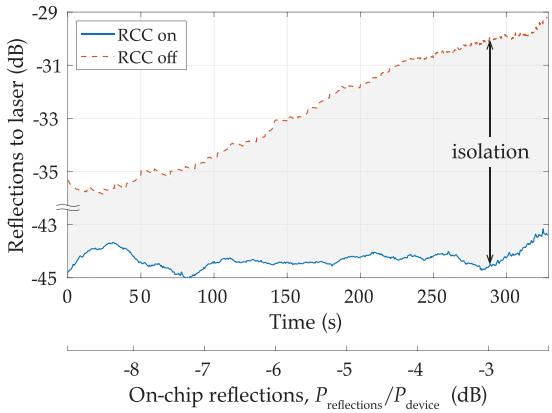

(b)

Fig. 11. (a) Experimental results of the dynamic cancellation part of the algorithm, indicating the power consumed by PS1 and PS2, and the photocurrent generated by PD1. (b) The reflections to the laser when varied with time, with the RCC off, and on, measured using PD1 (and calibrated to account for the setup and lensed-fiber-to-chip coupling loss). The lensed-fiber-to-chip coupling loss was $\sim$11 dB, and the PDs power taps had a power coupling ratio of $\sim$15%. These values were measured using on-chip PD1, on-chip PD4, and the off-chip PD (DC PD shown in Fig. 8).

to satisfy condition 6 of the algorithm. To measure the RCC's performance due to time-changing variable on-chip reflections, we conducted a dynamic test by varying the on-chip reflections from -9 to -2 dB (using the on-chip VOA shown in Fig. 9). PS1 and PS2 were locked, as shown in Fig. 11(a), to ensure that the photocurrent measured by PD1 is minimized and accordingly the reflections going back to the laser, as indicated in Fig. 11(a) and Fig. 11(b), respectively. The power consumed by PS1 and PS2 as well as the photocurrent measured by PD1 are shown in Fig. 11(a). The dynamic cancellation to minimize the optical power at PD1 was implemented using the gradient-descent minimization method described in ref. [48]. With the photocurrent measured by PD1 as the parameter to minimize, step size adjustments for PS1 and PS2 were determined by calculating their individual gradients, gi, multiplying by a scaling factor α (determined empirically), and shifting the tuning voltages by

α_{gi}. This minimization was continually left running to track the shifting minimum due to the sweeping of the reflected power, but depending on the application a threshold can be set below which the minimization is considered to be sufficient and the gradient-descent can be switched off.

The minimum photocurrent measured by PD1 when conducting the experiments was ∼90 nA (as shown in Fig. 11(a)). This means that the power going back to the inverse-taper edge coupler is ∼−30 dBm. It is worth mentioning that this amount of photocurrent was sufficient to stabilize the laser and narrow its linewidth. However, if the laser is integrated on-chip with minimal laser-to-waveguide coupling losses, the photocurrent measured by PD1 can be locked to a different value to ensure a stable laser operation and a narrow linewidth.

The total electrical power consumed by PS1 and PS2 from Fig. 11(a) is less than 75 mW. This is an overestimation of what the heaters would consume because MZI2 in our prototype was tuned between 25 mW (the MZI transmission's first null) and 55 mW (second maximum). If MZI2 was tuned between the first maximum and the second null, the total power consumed can be less than 45 mW, and can be further reduced if the heaters were implemented using doped silicon instead of TiN heaters located above the silicon waveguides [49]. Since the tapped optical power to the phase-tunable reflector will never exceed 3-dB (in the unlikely scenario of 100% reflections), and because broadband 3-dB couplers were used to form the tunable splitter/combiner, PS1 requires tuning over a $\pi/2$ phase range. Since since light passes twice through PS2, PS2 also require tuning over a $\pi/2$ phase range.

To monitor the laser performance in real-time due to the time-changing reflections in Fig. 11(b), we coupled −14 dB of the laser output power to an MZM (see Fig. 8). The MZM was modulated using a 10 Gb/s PRBS-7 signal and the modulated data was photodetected, split, and passed to an ED and an oscilloscope for measuring the bit errors and capturing the eye diagrams, respectively. Fig. 12 shows the bit errors (per second) as the on-chip reflections were varied. When the RCC was off, the bit errors became significant when the reflections to the laser ($P_{\text{fiber, in}}/P_{\text{fiber, out}}$) reached ∼ −34 dB. This is because at such a level (the total reflection going into the laser, $P_{\text{laser, in}}/P_{\text{laser, out}}$, was ∼−40 dB after accounting for the factory reported laser-to-fiber coupling loss of 50%), the laser enters the 'fourth' optical feedback regime where modes at the laser relaxation frequency start to appear [50], which increases the overall noise, eventually leading to a broadening of the laser linewidth and coherence collapse [51]. When the RCC was turned on, and as the on-chip reflections were varied between −9 dB and −2 dB, both the tunable splitter/combiner and the phase-tunable reflector were controlled simultaneously to minimize the photocurrent in PD1 to ∼90 nA. This reduced the reflections into the laser ($P_{\text{laser, in}}/P_{\text{laser, out}}$) to ∼−50 dB (including the laser-to-fiber coupling loss), which stabilized the laser by placing it in either the 'second' or 'third' optical feedback regime [45].

Fig. 11(b) and Fig. 12 show the resulting reflections to the laser (measured using PD1) when the on-chip reflections were changed deliberately as a function of time, for RCC off (i.e., the laser was unstable) and on (i.e., the laser was stable). The eye

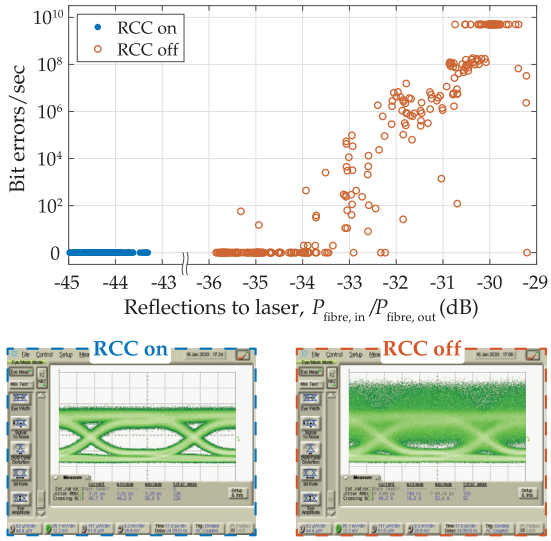

Fig. 12. The measured bit errors for a 10 Gb/s PRBS-7 signal as a function of the reflections to the laser ($P_{\text{fiber, in}}/P_{\text{fiber, out}}$) when the RCC was off and when it was on; both measurements used the same range of on-chip reflection ($P_{\text{reflections}}/P_{\text{device}}$) values, i.e., −9 dB to −2 dB. The eye diagrams shown were each captured over a duration of 330 seconds.

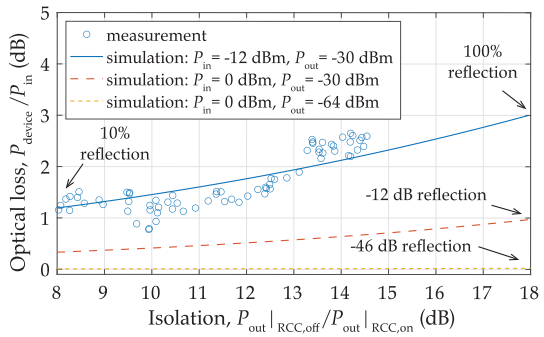

Fig. 13. The measured optical insertion loss ($P_{\text{device}}/P_{\text{in}}$) of the RCC (without the power taps losses) as a function of the optical isolation ($P_{\text{out}}|_{\text{RCC, off}}/P_{\text{out}}|_{\text{RCC, on}}$) measured using PD4. The solid lines are the simulation results for: 1) $P_{\text{in}} = -12$ dBm and $P_{\text{out}} = -30$ dBm (our case here), 2) $P_{\text{in}} = 0$ dBm and $P_{\text{out}} = -30$ dBm (if there are no setup and coupling losses), and 3) $P_{\text{in}} = 0$ dBm and $P_{\text{out}} = -64$ dBm (if there are no setup and coupling losses and the photocurrent read by PD1 was minimized to the minimum resolvable optical power of −73.7 dBm).

diagrams shown in Fig. 12 were taken over a duration of 330 seconds and show an unacceptably noisy eye when the RCC was off and an acceptable, clean eye when the RCC was on. Such a test indicates that the laser was stable throughout the time of conducting the experiment, despite the time-varying reflections.

The optical loss of the RCC ($P_{\text{device}}/P_{\text{in}}$) as a function of the isolation ratio ($P_{\text{out}}|_{\text{RCC, off}}/P_{\text{out}}|_{\text{RCC, on}}$) was measured using PD4 and is shown in Fig. 13. This is the dynamic loss, which can be expressed by Eq. (13), and thus excludes the excess loss of the fabricated power taps (∼1.4 dB), where the power taps had a measured power coupling ratio of ∼15% for each of the two power taps tapping optical power to PD1-4. In our design, we designed the power taps for a large power coupling strength of 10%, however, power taps with a smaller power coupling

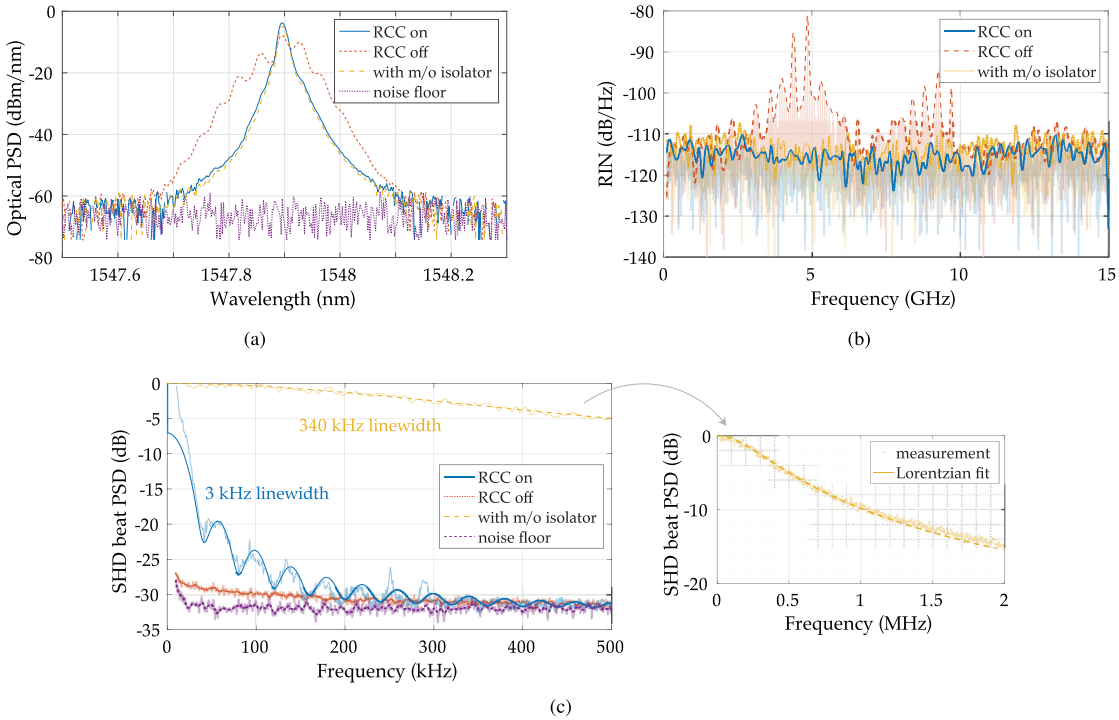

Fig. 14. The laser performance when the RCC was off, when the RCC was on, and with a magneto-optic isolator. (a) The optical spectrum of the laser. (b) The RIN of the laser (with 17 dB loss, hence the high instrument-limited noise floor, see Appendix D). The dark lines are the envelopes of the spectra and the light lines are the actual measurement results. (c) The self-homodyne (SHD) beat power spectral density (PSD) spectra indicating the linewidth of the laser. The light lines are the measured spectra and the dark lines are drawn fitting to the measurement results using theoretical models of the SHD beat PSD lineshapes (see Appendix C). The inset shows the spectrum for the case in which an isolator was used over a large frequency span.

strength (such as 1%) for lower losses (<0.1 dB) can also be used with the PDs used here (as explained in Section IV-A).

B. Laser Performance Characterization

To compare the laser performance to that with an isolator was used, the laser optical spectrum, RIN, and linewidth were measured simultaneously, using the setup shown in Fig. 8, after completing the dynamic tests but retaining the final values for the reflections into the laser for both the dynamic tests, i.e., $P_{\text{fiber, in}}/P_{\text{fiber, out}} \approx -29$ dB with the RCC off, and $P_{\text{fiber, in}}/P_{\text{fiber, out}} \approx -44$ dB with the RCC on. When the RCC was off, the optical spectrum in Fig. 14(a) shows a broadened optical spectrum and the appearance of sidebands at the laser relaxation oscillation frequency. These sidebands occur simultaneously as indicated by the peaks shown in the RIN spectrum in Fig. 14(b). The laser linewidth was also measured, as shown in Fig. 14(c), using the SHD technique (see Appendix C for details) and shows a beat PSD that is close to the RFSA noise floor when the RCC was off, indicating the broadening of the laser linewidth. When the RCC was on, the optical spectrum showed a single lasing peak, see Fig. 14(a). To compare the performance of the laser with the RCC to a laser with an isolator, we added a fiber-optic magneto-optic isolator to the laser. The optical spectrum and the RIN of the laser when the RCC was on is comparable to when the isolator was used. However, the linewidth of the laser was reduced to ∼3 kHz with the RCC on, compared to 340 kHz with the magneto-optic isolator, which is due to the feedback-induced linewidth reduction [45]. It is worth mentioning that the linewidth of the laser measured with the magneto-optic isolator is about 10% of the factory reported linewidth of the free-running laser, ∼3 MHz, which is due to reflections from the fiber connectors and the fiber [7]. This means, by locking the RCC to send back ∼−44 dB of optical power to the laser [55], the free-running laser linewidth was reduced by more than two orders of magnitude.

VII. Discussion and Conclusion

We demonstrated an RCC that ensures the stable operation of a laser by canceling coherent back reflections. In our demonstration, we used an on-chip variable attenuator with a single-point reflector and showed the dynamic laser stabilization due to slowly varying on-chip back reflections amplitude and phase. In practical systems, reflections can change more rapidly. As long as the variation in the reflections amplitude or phase (or both) is slower than the control loop's response time, the RCC can be used to cancel those reflections. In our demonstration, the loop response time/bandwidth was limited by the data acquisition time using the implemented control scheme (around 16 ms, measured as the difference in time between setting a specific bias to the heaters and reading power from the SMU). For faster changing reflections, a dedicated control electronic circuit can be used and the thermal heaters can be replaced by faster tuners, such as p-n junctions.

TABLE II
COMPARISON OF DIFFERENT ISOLATION METHODS FOR THE TE MODE, IN THE C BAND, ON SILICON PLATFORM

Method	Reference	Isolation (dB)	Loss (dB)
Magneto-optics using monolithic Ce:YIG	[52]	11	4
	[53]	30	9
Traveling-wave modulator	[21]	3	-
Tandem phase modulator	[22]	3	2
Nonlinearity using four-wave mixing	[54]	4	-
	[17]	18	4
	[16]	25	19
Reflection-cancellation (our work)	demonstrated	16	3.5
	optimized	64	< 0.5

In practice, multiple reflection points can exist on chip. In such a case, the total reflections going back to the laser will have a spectrum similar to that of the reflection port of a Fabry-Perot interferometer (in the case of large reflections amplitudes), where there will be a certain amplitude and phase of the light going back to the laser that the RCC should be able to cancel. Although in conducting our experiments, the total reflections included both the on-chip reflector and the grating coupler's reflections, we confirmed the RCC functionality due to multiple large reflections point by simulating the laser temporal response due to two reflection points, and showed the successful stabilization of the laser (see Appendix A for simulations details).

Further more, in practical communication systems, on-chip transmitters can result in frequency-shifted back reflections due to the time-dependent fluctuations. Such reflections might result in injection pulling (which increases the laser noise), depending on the magnitude and detuning of these frequency-shifted signals from the laser's optical frequency [56]. While such effects on the RCC and the laser were not studied here, adding a high quality-factor filter (centered at the laser optical frequency) after (or before) the RCC can filter such frequencies.

The RCC demonstrated here can also be used to stabilize integrated lasers by deliberately reflecting larger optical amplitudes back to the laser, thus putting the laser in the stable 'fifth' optical feedback regime [7], [57]. This can help in stabilizing the laser against remote reflections occurring downstream in the fiber link [32]. In our demonstration here, we locked the laser in the 'second' or 'third' optical feedback regimes because of the setup and fiber-to-chip coupling losses (see Fig. 9).

It is worth noting that, when lasers are integrated on a chip, back reflections typically occur with a delay shorter than what we presented here (due to the optical fibers connecting the laser to the chip). If such delays are shorter than the inverse of the laser relaxation frequency, stronger feedback is required to transition the laser to the unstable 'fourth' regime [58]. Here we showed the lowest feedback levels (most stringent case) for which the RCC was able to stabilize the laser. This also relaxes the design constraint for very low return-loss RCC devices (directional couplers and PDs). Since the laser is more tolerant to larger optical feedback levels from closer devices (such as when they are integrated on-chip) [58], the RCC components do not necessarily need to be designed with extremely low return losses.

Table II compares our work to some of the reported on-Si isolators based on alternative methods. The most common dynamic non-reciprocal nonlinear-based isolators use four-wave mixing techniques and thus rely on a high-power external pump signal with moderate levels of isolation and large losses [16], [17], [54]. Isolators based on spatio-temporal modulation were demonstrated either using traveling-wave MZMs [21], [23] or tandem phase modulators [22]. Both methods involve high-speed circuits, consume a large footprint, and resulted in moderate levels of isolation. Magneto-optical materials (such as Ce:YIG) monolithically integrated on Si are usually realized using an interferometer, such as a Mach-Zehnder interferometer [53] or a microring resonator [59] as the isolation is based on the nonreciprocal phase shift. This usually results in high losses [53]. In addition, since interferometers are used, they also require active tuning to combat temperature variations. Our RCC, however, does not require an external pump signal, any changes to the fabrication process, specifically without the deposition of any additional materials, and can provide up to 64 dB of isolation/cancellation (limited by the PDs minimum detectable power; in Table II, the demonstrated isolation was limited by the 12 dB optical coupling loss between the lensed fiber and the SiP chip), and has a low insertion loss (in Table II, the demonstration had a loss of $\sim$1.4 dB attributed to the PDs power taps). The estimated loss of the RCC including the 10% power taps is less than 1.5 dB for moderate reflections smaller than -20 dB. If 1% power taps are used, the loss would be 0.5 dB for reflections smaller than -20 dB. Besides isolating the laser from reflections, the RCC improves the laser performance by accurately locking its operation in a stable optical feedback regime, further reducing its linewidth to 3 kHz. The latter is important for enabling several applications including coherent communication [60], spectroscopy, and atomic clocks [61], and frequency-modulated continuous-wave lidars. Our results pave the way towards the deployment and scaling of fully-integrated electronic-photonic silicon chips at a low cost using zero-change CMOS foundry processes.

APPENDIX A
MULTI-POINT REFLECTIONS MODEL

The same model described in Eq. (2) was used to confirm the laser stabilization due to the RCC in the case of multiple reflection points. In such a case, the optical feedback term is

written as

$$F(t) = \frac{1}{\tau_D}\frac{1-R_2}{\sqrt{R_2}}\left(-F_0(t) + F_1(t) + F_2(t)\right), \tag{16a}$$

$$F_0(t) = E(t-\tau_0)\kappa b e^{j\omega_0\tau_0}e^{j\phi_b}, \tag{16b}$$

$$F_1(t) = E(t-\tau_1)(1-\kappa)a e^{j\omega_0\tau_1}e^{j\phi_a}, \tag{16c}$$

$$F_2(t) = E(t-\tau_2)(1-\kappa)(1-a^2)c e^{j\omega_0\tau_2}e^{j\phi_c}, \tag{16d}$$

where $F_2(t)$ represents the optical feedback due to the second reflection point of fields amplitude of c and phase of ϕ_c. It is worth mentioning that the optical feedback in Eq. (6) and Eq. (16) was derived assuming weak reflection amplitudes [33]. In the case of strong reflections, the higher order terms that were neglected in our derivations shall be considered, as described in ref. [37]. It is worth mentioning that the stability of the laser due to the RCC is dependent on the distance between the laser and the reflection points, L_0 and L_1 as explained in [32]. Conducting a similar analysis to that described in [32], [62], using the parameters in Table I, the RCC is expected to stabilize the laser against reflections up to several centimeters away from the laser.

Appendix B
Photodetector Characterization

For the SiGe PDs used in the RCC, we measured the dark current noise and the responsivity. Fig. 15(a) shows the dark current distribution at a bias of -1 V, where the average dark current was $I_{\text{dark}} = 5.14$ nA and the dark current noise, $I_{\text{noise}} = 34.1$ pA (using the root-mean-square deviation of the measured dark current noise from the root-mean-square dark current) [42]. Fig. 15(b) shows a responsivity of $\mathcal{R} = 0.8$ A/W (at a bias of -1 V), which is measured by splitting the light going to the PD and measuring it using an on-chip grating coupler.

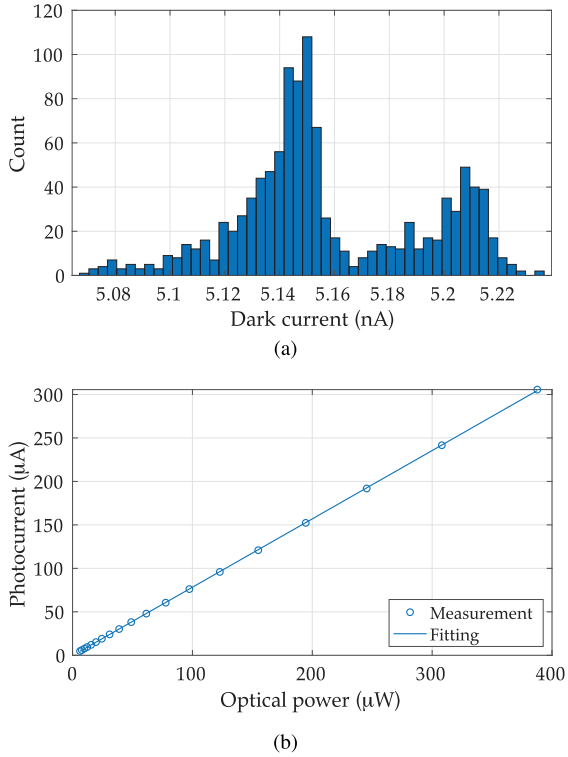

Fig. 15. Photodetector characterization results. (a) Measured dark current noise of the SiGe PDs used in the RCC (and including the SMU noise). 1121 samples of the dark current were collected over 600 seconds over an integration time of 0.5 seconds (1 Hz) per dark current measurement. (b) Measured responsivity of the SiGe PDs used in the RCC. The circles are the measurement data and the solid line is a linear fitting. The responsivity is 0.8 A/W.

Appendix C
Linewidth Measurement

The laser linewidth was measured by the SHD technique using the setup shown in Fig. 8. An Agilent 11980 A interferometer, which had a delay (τ_0) of 25 μs (5.2 km of optical fiber) between the unbalanced MZI arms, was used. This enabled the measurement of laser linewidth of 32 kHz and above. For the case in which a magneto-optic isolator was attached to the laser, the Lorentzian function,

$$S(f) = A\frac{P_0^2}{4\pi}\frac{\Delta f^2}{f^2+\Delta f^2}, \tag{17}$$

where A is a scaling factor, P_0 is the laser power, f is the frequency spectrum, and Δf is the laser linewidth, was fit to normalized SHD beat PSD. This yielded $\Delta f = 340$ kHz. For the case in which the RCC was on, the power ratio going into the laser is ~ -50 dB. This reduced the laser linewidth as revealed in the sub-coherent SHD beat PSD shown in Fig. 14(c), which happens if the unbalanced interferometer has a delay less than $5/2\pi\Delta f$. In such a case, the sub-coherent lineshape function given by [63]

$$\begin{aligned} S(f) = {} & A\frac{\frac{1}{2}P_0^2\tau_c}{1+(2\pi f)^2\tau_c^2} \\ & \times\left[1 - e^{-\tau_0/\tau_c}\left[\cos(2\pi f\tau_0) + \frac{\sin(2\pi f\tau_0)}{2\pi f\tau_0}\right]\right] \\ & + \frac{1}{2}P_0^2\pi e^{-\tau_0/\tau_c}\delta(2\pi f) + N(f), \end{aligned} \tag{18}$$

which can be fit to the SHD beat PSD to extract Δf. Here, $\tau_c = 1/(2\pi\Delta f)$ is the laser coherence time, and $N(f)$ is the measurement noise shown in Fig. 14(c). Fitting Eq. (18) to the SHD beat PSD when the RCC is on, results in $\Delta f = 3$ kHz.

Appendix D
RIN Spectrum Measurement

The RIN spectrum was measured by subtracting the measured thermal noise spectrum and the shot noise term from the total measured noise spectrum. Since the optical power going to the Agilent 71400 C lightwave signal analyzer is $\sim$17 dB lower than the laser output power, the RIN shown in Fig. 14(b) is overestimated. The actual RIN of the laser, measured using an isolator, is shown in Fig. 16. However, we report the RIN in Fig. 14(b) to show the difference between the laser noise spectrum when the RCC is on and when the RCC is off, and

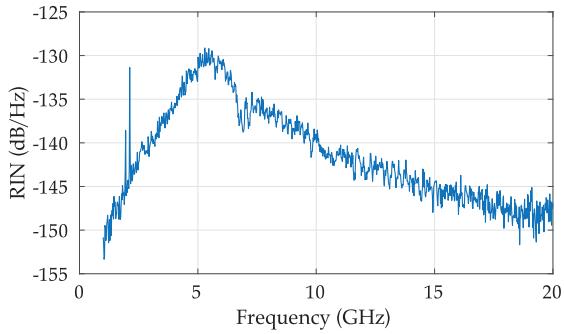

Fig. 16. RIN of the QWDFB laser with a magneto-optic isolator. The RIN peaks to −129 dB/Hz at 5.5 GHz.

compare it to the case in which a magneto-optic isolator was used.

ACKNOWLEDGMENT

The authors thank Mustafa Hamood for his help with designing the PCB, Ahmed Atef Ali of UBC and Ranjeet Kumar, Duanni Huang, Meer Sakib, and Chaoxuan Ma of Intel for the helpful discussions and feedback. Access to fabrication and design tools were provided by CMC microsystems.

REFERENCES

[1] C. Sun *et al.* "Single-chip microprocessor that communicates directly using light," *Nature*, vol. 528, no. 7583, pp. 534–538, 2015.
[2] A. H. Atabaki *et al.* "Integrating photonics with silicon Nanoelectronics for the next generation of systems on a chip," *Nature*, vol. 556, no. 7701, pp. 349–354, 2018.
[3] G. Zhang *et al.* "An integrated silicon photonic chip platform for continuous-variable quantum key distribution," *Nature Photon.*, vol. 13, no. 12, pp. 839–842, 2019.
[4] X. Qiang *et al.* "Large-scale silicon quantum photonics implementing arbitrary two-Qbit processing," *Nature Photon.*, vol. 12, no. 9, pp. 534–539, 2018.
[5] D. Jalas *et al.* "What is -and what is not- an optical isolator," *Nature Photon.*, vol. 7, no. 8, pp. 579–582, 2013.
[6] R. Tkach and A. Chraplyvy, "Regimes of feedback effects in 1.5-μm distributed feedback lasers," *J. Lightw. Technol.*, vol. 4, no. 11, pp. 1655–1661, Nov. 1986.
[7] N. Schunk and K. Petermann, "Numerical analysis of the feedback regimes for a single-mode semiconductor laser with external feedback," *IEEE J. Quantum Electron.*, vol. 24, no. 7, pp. 1242–1247, Jul. 1988.
[8] L. Bi *et al.*, "On-chip optical isolation in Monolithically integrated non-reciprocal optical resonators," *Nature Photon.*, vol. 5, no. 12, p. 758, 2011.
[9] M.-C. Tien, T. Mizumoto, P. Pintus, H. Kromer, and J. E. Bowers, "Silicon ring isolators with bonded nonreciprocal magneto-optic garnets," *Opt. Exp.*, vol. 19, no. 12, pp. 11 740–11 745, 2011.
[10] D. Huang, P. Pintus, C. Zhang, Y. Shoji, T. Mizumoto, and J. E. Bowers, "Electrically driven and thermally tunable integrated optical isolators for silicon photonics," *IEEE J. Sel. Topics Quantum Electron.*, vol. 22, no. 6, pp. 271–278, Nov./Dec. 2016.
[11] T. Mizumoto, R. Baets, and J. E. Bowers, "Optical nonreciprocal devices for silicon Photonics using wafer-bonded magneto-optical garnet materials," *MRS Bull.*, vol. 43, no. 6, pp. 419–424, 2018.
[12] M. Krause, H. Renner, and E. Brinkmeyer, "Optical isolation in silicon waveguides based on nonreciprocal raman amplification," *Electron. Lett.*, vol. 44, no. 11, pp. 691–693, 2008.
[13] L. Fan *et al.*, "An all-silicon passive optical diode," *Science*, vol. 335, no. 6067, pp. 447–450, 2012.
[14] Z. Wu *et al.*, "Optical nonreciprocal transmission in an asymmetric silicon photonic crystal structure," *Appl. Phys. Lett.*, vol. 107, no. 22, 2015, Art. no. 221102.
[15] C.-H. Dong, Z. Shen, C.-L. Zou, Y.-L. Zhang, W. Fu, and G.-C. Guo, "Brillouin-scattering-induced transparency and non-reciprocal light storage," *Nature Commun.*, vol. 6, no. 1, pp. 1–6, 2015.
[16] K. Wang *et al.*, "Four-wave-mixing-based silicon integrated optical isolator with dynamic non-reciprocity," *IEEE Photon. Technol. Lett.*, vol. 28, no. 16, pp. 1739–1742, Aug. 2016.
[17] S. Hua, J. Wen, X. Jiang, Q. Hua, L. Jiang, and M. Xiao, "Demonstration of a chip-based optical isolator with parametric amplification," *Nature Commun.*, vol. 7, no. 1, pp. 1–6, 2016.
[18] A. Li and W. Bogaerts, "Reconfigurable nonlinear nonreciprocal transmission in a silicon photonic integrated circuit," *Optica*, vol. 7, no. 1, pp. 7–14, 2020.
[19] K. Y. Yang *et al.* "Inverse-designed non-reciprocal pulse router for chip-based lidar," *Nature Photon.*, vol. 14, no. 6, pp. 369–374, 2020.
[20] Z. Yu and S. Fan, "Complete optical isolation created by indirect interband photonic transitions," *Nature Photon.*, vol. 3, no. 2, pp. 91–94, 2009.
[21] H. Lira, Z. Yu, S. Fan, and M. Lipson, "Electrically driven nonreciprocity induced by interband photonic transition on a silicon chip," *Phys. Rev. Lett.*, vol. 109, no. 3, 2012, Art. no. 0 33901.
[22] C. Doerr, L. Chen, and D. Vermeulen, "Silicon Photonics broadband modulation-based isolator," *Opt. Exp.*, vol. 22, no. 4, pp. 4493–4498, 2014.
[23] P. Dong, "Travelling-wave Mach-Zehnder modulators functioning as optical isolators," *Opt. Exp.*, vol. 23, no. 8, pp. 10498–10505, 2015.
[24] D. B. Sohn, S. Kim, and G. Bahl, "Time-reversal symmetry breaking with acoustic pumping of nanophotonic circuits," *Nature Photon.*, vol. 12, no. 2, pp. 91–97, 2018.
[25] Y. Shi, Z. Yu, and S. Fan, "Limitations of nonlinear optical isolators due to dynamic reciprocity," *Nature Photon.*, vol. 9, no. 6, pp. 388–392, 2015.
[26] N. Chinone, K. Aiki, and R. Ito, "Stabilization of semiconductor laser outputs by a mirror close to a laser facet," *Appl. Phys. Lett.*, vol. 33, no. 12, pp. 990–992, 1978.
[27] P. Alipour, A. A. Eftekhar, A. H. Atabaki, and A. Adibi, "Thermally reconfigurable device for adaptive reflection suppression on a silicon-on-insulator platform," *Opt. Lett.*, vol. 39, no. 5, pp. 1141–1144, 2014.
[28] T. W. Baehr-Jones, M. A. Streshinsky, Y. Liu, M. J. Hochberg, R. Ding, and A. Tager, "Controlling back scattering in optical waveguide systems," U.S. Patent 10133014, Nov. 20, 2018.
[29] J. Bovington, "Optical device with reduced back reflection," U.S. Patent 10365432, Jul. 30, 2019.
[30] L. Tang, J. Li, S. Yang, H. Chen, and M. Chen, "A method for improving reflection tolerance of laser source in hybrid Photonic packaged micro-system," *IEEE Photon. Technol. Lett.*, vol. 33, no. 9, pp. 465–468, May 2021.
[31] S. Shao, J. Li, Y. Wu, S. Yang, H. Chen, and M. Chen, "Modulation bandwidth enhanced self-injection locking laser with an external high-Q microring reflector," *Opt. Lett.*, vol. 46, no. 13, pp. 3251–3254, 2021.
[32] J. Hauck *et al.*, "Stabilization and frequency control of a DFB laser with a tunable optical reflector integrated in a silicon photonics PIC," *J. Lightw. Technol.*, vol. 34, no. 23, pp. 5467–5473, 2016.
[33] H. Shoman, "Reconfigurable silicon photonic integrated circuits," Ph.D. dissertation, Department of Electrical and Computer Engineering, Univ. British Columbia, Oct. 2020.
[34] R. Lang and K. Kobayashi, "External optical feedback effects on semiconductor injection laser properties," *IEEE J. Quantum Electron.*, vol. QE-16, no. 3, pp. 347–355, Mar. 1980.
[35] N. Schunk and K. Petermann, "Noise analysis of injection-locked semiconductor injection lasers," *IEEE J. Quantum Electron.*, vol. QE-22, no. 5, pp. 642–650, May 1986.
[36] R. L. Burden and D. J. Faires, "Numerical analysis," Brooks/Cole, 2011.
[37] K. I. Kallimani and M. O'mahony, "Relative intensity noise for laser diodes with arbitrary amounts of optical feedback," *IEEE J. Quantum Electron.*, vol. 34, no. 8, pp. 1438–1446, Aug. 1998.
[38] H. Packard, *Lightwave Signal Analysers Measure Relative Intensity Noise.* Palo Alto, CA, USA: Hewlett-Packard, 1991.
[39] H. Yun, W. Shi, Y. Wang, L. Chrostowski, and N. A. F. Jaeger, "2 × 2 adiabatic 3-dB coupler on silicon-on-insulator rib Waveguides," in *Proc. Photon. North Int. Soc. Opt. Photon.*, 2013, Art. no. 89150V.
[40] Y. Zhang *et al.*, "A compact and low loss Y-junction for submicron silicon Waveguide," *Opt. Exp.*, vol. 21, no. 1, pp. 1310–1316, 2013.
[41] T.-Y. Liow *et al.*, "Silicon modulators and germanium Photodetectors on SOI: Monolithic integration, compatibility, and performance optimization," *IEEE J. Sel. Topics Quantum Electron.*, vol. 16, no. 1, pp. 307–315, Jan./Feb. 2010.

[42] X. An, F. Liu, Y. J. Jung, and S. Kar, "Tunable Graphene-silicon Heterojunctions for Ultrasensitive Photodetection," *Nano Lett.*, vol. 13, no. 3, pp. 909–916, 2013.
[43] W. Bogaerts and S. K. Selvaraja, "Compact single-mode silicon hybrid rib/strip waveguide with adiabatic bends," *IEEE Photon. J.*, vol. 3, no. 3, pp. 422–432, Jun. 2011.
[44] V. Mackowiak, J. Peupelmann, Y. Ma, and A. Gorges, "NEP-Noise equivalent power," Thorlabs, Inc., Newton, NJ, USA, White Paper, 2015.
[45] K. Kikuchi and T. Okoshi, "Simple formula giving spectrum-narrowing ratio of semiconductor-laser output obtained by optical feedback," *Electron. Lett.*, vol. 18, no. 1, pp. 10–12, 1982.
[46] "Fab: Advanced micro foundry (AMF) silicon Photonics fabrication process," Accessed: Apr. 07, 2020. [Online]. Available: https://www.cmc.ca/en/WhatWeOffer/Products/CMC-00200-03001.aspx
[47] Z. Lu *et al.*, "Broadband silicon Photonic directional coupler using asymmetric-waveguide based phase control," *Opt. Exp.*, vol. 23, no. 3, pp. 3795–3808, 2015.
[48] M. Ma, H. Shoman, K. Tang, S. Shekhar, N. A. Jaeger, and L. Chrostowski, "Automated control algorithms for silicon Photonic polarization receiver," *Opt. Exp.*, vol. 28, no. 2, pp. 1885–1896, 2020.
[49] H. Jayatilleka, H. Shoman, L. Chrostowski, and S. Shekhar, "Photoconductive heaters enable control of large-scale silicon Photonic ring resonator circuits," *Optica*, vol. 6, no. 1, pp. 84–91, 2019.
[50] R. Miles, A. Dandridge, A. Tveten, H. Taylor, and T. Giallorenzi, "Feedback-induced line broadening in CW channel-substrate planar laser diodes," *Appl. Phys. Lett.*, vol. 37, no. 11, pp. 990–992, 1980.
[51] D. Lenstra, B. Verbeek, and A. Den Boef, "Coherence collapse in single-mode semiconductor lasers due to optical feedback," *IEEE J. Quantum Electron.*, vol. 21, no. 6, pp. 674–679, Jun. 1985.
[52] C. Zhang, P. Dulal, B. J. Stadler, and D. C. Hutchings, "Monolithically-integrated TE-mode 1D silicon-on-insulator isolators using Seedlayer-free garnet," *Sci. Rep.*, vol. 7, no. 1, pp. 1–8, 2017.
[53] Y. Zhang *et al.* "Monolithic integration of broadband optical isolators for polarization-diverse silicon Photonics," *Optica*, vol. 6, no. 4, pp. 473–478, 2019.
[54] K. Saha, Y. Okawachi, O. Kuzucu, M. Menard, M. Lipson, and A. L. Gaeta, "Chip-Scale broadband optical isolation via Bragg scattering four-wave mixing," in *Proc. CLEO: QELS_Fundam. Sci. Opt. Soc. Amer.*, 2013, Art. no. QF 1D-2.
[55] D. R. Hjelme, A. R. Mickelson, and R. G. Beausoleil, "Semiconductor laser stabilization by external optical feedback," *IEEE J. Quantum Electron.*, vol. 27, no. 3, pp. 352–372, Mar. 1991.
[56] K. Petermann, *Laser Diode Modulation and Noise*. Berlin, Germany: Springer, 2012.
[57] A. Mokhtar, L. MacEachern, and S. Mahmoud, "Isolator-free DFB laser diode operating in feedback regime V," in *Proc. Active Passive Opt. Compon. Commun. VI*, vol. 6389, 2006, Art. no. 63891F.
[58] N. Schunk and K. Petermann, "Stability analysis for laser diodes with short external cavities," *IEEE Photon. Technol. Lett.*, vol. 1, no. 3, pp. 49–51, Mar. 1989.
[59] D. Huang *et al.*, "Dynamically reconfigurable integrated optical circulators," *Optica*, vol. 4, no. 1, pp. 23–30, 2017.
[60] A. Ahmed, D. ElmoznineY. LimA. MaRylyakov, and S. Shekhar, "A dual-polarization silicon-photonic coherent transmitter supporting 552 Gb/s/wavelength," *IEEE J. Solid-State Circuits*, vol. 55, no. 9, pp. 2597–2608, Sep. 2020.
[61] M. H. Idjadi and F. Aflatouni, "Nanophotonic phase noise filter in silicon," *Nature Photon.*, vol. 14, no. 4, pp. 234–239, 2020.
[62] J. Ohtsubo, *Semiconductor Lasers: Stability, Instability and Chaos*. Berlin, Germany: Springer, 2012.
[63] L. Richter, H. Mandelberg, M. Kruger, and P. McGrath, "Linewidth determination from self-heterodyne measurements with Subcoherence delay times," *IEEE J. Quantum Electron.*, vol. QE-22, no. 11, pp. 2070–2074, Nov. 1986.